Supporting Information for "Dilution of boundary layer cloud condensation nucleus concentrations by free tropospheric entrainment during marine cold air outbreaks"

F. Tornow[1,2], A. S. Ackerman[2], A. M. Fridlind[2], B. Cairns[2], E. C. Crosbie[3,4], S. Kirschler[5,6], R. H. Moore[3], D. Painemal[3,4], C. E. Robinson[3,4], C. Seethala[7], M. A. Shook[3], C. Voigt[5,6], E. L. Winstead[3,4], L. D. Ziemba[3], P. Zuidema[7], A. Sorooshian[8,9]

[1]Earth Institute, Columbia University, NY, 10025, NY

[2]NASA Goddard Institute for Space Studies, NY, 10025, NY

[3]NASA Langley Research Center, Hampton, VA 23681, USA

[4]Science, Systems, and Applications, Inc., Hampton, VA 23681, USA

[5]Deutsches Zentrum für Luft- und Raumfahrt (DLR), Oberpfaffenhofen, Germany

[6]Johannes Gutenberg-Universität, Mainz, Germany

[7]Rosenstiel School of Marine and Atmosphere Science, University of Miami, FL, 33149, USA

[8]Department of Chemical and Environmental Engineering, University of Arizona, Tucson, Arizona, 85721, USA

[9]Department of Hydrology and Atmospheric Sciences, University of Arizona, Tucson, Arizona, 85721, USA

Contents of this file

---

1. Methodology

2. Figures S1 to S9

3. Tables S1 to S2

References

Atkinson, B. W., & Wu Zhang, J. (1996). Mesoscale shallow convection in the atmosphere. *Reviews of Geophysics*, *34*(4), 403-431. Retrieved from https://agupubs.onlinelibrary.wiley.com/doi/abs/10.1029/96RG02623 doi: https://doi.org/10.1029/96RG02623

Burton, S. P., Hostetler, C. A., Cook, A. L., Hair, J. W., Seaman, S. T., Scola, S., … Müller, D. (2018, Jul). Calibration of a high spectral resolution lidar using a michelson interferometer, with data examples from oracles. *Appl. Opt.*, *57*(21), 6061–6075. Retrieved from http://www.osapublishing.org/ao/abstract.cfm?URI=ao-57-21-6061 doi: 10.1364/AO.57.006061

Böhm, J. P. (1992). A general hydrodynamic theory for mixed-phase microphysics. part i: drag and fall speed of hydrometeors. *Atmospheric Research*, *27*(4), 253-274. Retrieved from https://www.sciencedirect.com/science/article/pii/0169809592900359 doi: https://doi.org/10.1016/0169-8095(92)90035-9

Cairns, B., Russell, E. E., & Travis, L. D. (1999). Research Scanning Polarimeter: calibration and ground-based measurements. In D. H. Goldstein & D. B. Chenault (Eds.), *Polarization: Measurement, analysis, and remote sensing ii* (Vol. 3754, pp. 186 – 196). SPIE. Retrieved from https://doi.org/10.1117/12.366329 doi: 10.1117/12.366329

Dadashazar, H., Braun, R. A., Crosbie, E., Chuang, P. Y., Woods, R. K., Jonsson, H. H., & Sorooshian, A. (2018). Aerosol characteristics in the entrainment interface layer in relation to the marine boundary layer and free troposphere. *Atmospheric Chemistry and Physics*, *18*(3), 1495–1506. Retrieved from https://acp.copernicus.org/articles/18/1495/2018/ doi: 10.5194/acp-18-1495-2018

DeCarlo, P. F., Dunlea, E. J., Kimmel, J. R., Aiken, A. C., Sueper, D., Crounse, J., … Jimenez, J. L. (2008). Fast airborne aerosol size and chemistry measurements above mexico city and central mexico during the milagro campaign. *Atmospheric Chemistry and Physics*, *8*(14), 4027–4048. Retrieved from https://acp.copernicus.org/articles/8/4027/2008/ doi: 10.5194/acp-8-4027-2008

Etling, D., & Brown, R. A. (1993). Roll vortices in the planetary boundary layer: A review. *Boundary-Layer Meteorology*, *65*(3), 215–248. Retrieved from https://link.springer.com/article/10.1007/BF00705527 doi: 10.1007/BF00705527

Fridlind, A. M., Ackerman, A. S., Chaboureau, J.-P., Fan, J., Grabowski, W. W., Hill, A. A., … Zhang, M. (2012). A comparison of twp-ice observational data with cloud-resolving model results. *Journal of Geophysical Research: Atmospheres*, *117*(D5). Retrieved from https://agupubs.onlinelibrary.wiley.com/doi/abs/10.1029/2011JD016595 doi: 10.1029/2011JD016595

Froyd, K. D., Murphy, D. M., Brock, C. A., Campuzano-Jost, P., Dibb, J. E., Jimenez, J.-L., … Ziemba, L. D. (2019). A new method to quantify mineral dust and other aerosol species from aircraft platforms using single-particle mass spectrometry. *Atmospheric Measurement Techniques*, *12*(11), 6209–6239. Retrieved from https://

amt.copernicus.org/articles/12/6209/2019/ doi: 10.5194/amt-12-6209-2019

Hall, W. D. (1980). A detailed microphysical model within a two-dimensional dynamic framework: Model description and preliminary results. *Journal of Atmospheric Sciences*, *37*(11), 2486 - 2507. Retrieved from https://journals.ametsoc.org/view/journals/atsc/37/11/1520-0469_1980_037_2486_admmwa_2_0_co_2.xml doi: 10.1175/1520-0469(1980)037⟨2486:ADMMWA⟩2.0.CO;2

Hock, T. F., & Franklin, J. L. (1999). The ncar gps dropwindsonde. *Bulletin of the American Meteorological Society*, *80*(3), 407 - 420. Retrieved from https://journals.ametsoc.org/view/journals/bams/80/3/1520-0477_1999_080_0407_tngd_2_0_co_2.xml doi: 10.1175/1520-0477(1999)080⟨0407:TNGD⟩2.0.CO;2

Kleine, J., Voigt, C., Sauer, D., Schlager, H., Scheibe, M., Jurkat-Witschas, T., ... Anderson, B. E. (2018). In situ observations of ice particle losses in a young persistent contrail. *Geophysical Research Letters*, *45*(24), 13,553-13,561. Retrieved from https://agupubs.onlinelibrary.wiley.com/doi/abs/10.1029/2018GL079390 doi: https://doi.org/10.1029/2018GL079390

Knop, I., Bansmer, S. E., Hahn, V., & Voigt, C. (2021). Comparison of different droplet measurement techniques in the braunschweig icing wind tunnel. *Atmospheric Measurement Techniques*, *14*(2), 1761–1781. Retrieved from https://amt.copernicus.org/articles/14/1761/2021/ doi: 10.5194/amt-14-1761-2021

Lance, S., Nenes, A., Medina, J., & Smith, J. N. (2006a). Mapping the operation of the dmt continuous flow ccn counter. *Aerosol Science and Technology*, *40*(4), 242-

254. Retrieved from https://doi.org/10.1080/02786820500543290 doi: 10.1080/02786820500543290

Lance, S., Nenes, A., Medina, J., & Smith, J. N. (2006b). Mapping the operation of the dmt continuous flow ccn counter. *Aerosol Science and Technology*, *40*(4), 242-254. Retrieved from https://doi.org/10.1080/02786820500543290 doi: 10.1080/02786820500543290

Lawson, R. P., O'Connor, D., Zmarzly, P., Weaver, K., Baker, B., Mo, Q., & Jonsson, H. (2006). The 2d-s (stereo) probe: Design and preliminary tests of a new airborne, high-speed, high-resolution particle imaging probe. *Journal of Atmospheric and Oceanic Technology*, *23*(11), 1462 - 1477. Retrieved from https://journals.ametsoc.org/view/journals/atot/23/11/jtech1927_1.xml doi: 10.1175/JTECH1927.1

Li, X.-Y., Wang, H., Chen, J., Endo, S., George, G., Cairns, B., ... Zuidema, P. (2021). Large-eddy simulations of marine boundary-layer clouds associated with cold air outbreaks during the activate campaign– part 1: Case setup and sensitivities to large-scale forcings. *Journal of the Atmospheric Sciences*. Retrieved from https://journals.ametsoc.org/view/journals/atsc/aop/JAS-D-21-0123.1/JAS-D-21-0123.1.xml doi: 10.1175/JAS-D-21-0123.1

Lilly, D. K. (1968). Models of cloud-topped mixed layers under a strong inversion. *Quarterly Journal of the Royal Meteorological Society*, *94*(401), 292-309. Retrieved from https://rmets.onlinelibrary.wiley.com/doi/abs/10.1002/qj.49709440106 doi: https://doi.org/10.1002/qj.49709440106

Moore, R. H., & Nenes, A. (2009). Scanning flow ccn analysis—a method for fast measurements of ccn spectra. *Aerosol Science and Technology*, *43*(12), 1192-1207. Retrieved from https://doi.org/10.1080/02786820903289780 doi: 10.1080/02786820903289780

Moore, R. H., Thornhill, K. L., Weinzierl, B., Sauer, D., D'Ascoli, E., Kim, J., ... Anderson, B. E. (2017). Biofuel blending reduces particle emissions from aircraft engines at cruise conditions. *Nature*, *543*, 411-415. Retrieved from https://www.nature.com/articles/nature21420 doi: 10.1038/nature21420

Noh, Y.-J., Seaman, C. J., Haar, T. H. V., & Liu, G. (2013). In situ aircraft measurements of the vertical distribution of liquid and ice water content in midlatitude mixed-phase clouds. *Journal of Applied Meteorology and Climatology*, *52*(1), 269 - 279. Retrieved from https://journals.ametsoc.org/view/journals/apme/52/1/jamc-d-11-0202.1.xml doi: 10.1175/JAMC-D-11-0202.1

Roberts, G. C., & Nenes, A. (2005). A continuous-flow streamwise thermal-gradient ccn chamber for atmospheric measurements. *Aerosol Science and Technology*, *39*(3), 206-221. Retrieved from https://doi.org/10.1080/027868290913988 doi: 10.1080/027868290913988

Rolph, G., Stein, A., & Stunder, B. (2017). Real-time environmental applications and display system: Ready. *Environmental Modelling & Software*, *95*, 210-228. Retrieved from https://www.sciencedirect.com/science/article/pii/S1364815217302360 doi: https://doi.org/10.1016/j.envsoft.2017.06.025

Seethala, C., Zuidema, P., Edson, J., Brunke, M., Chen, G., Li, X.-Y., ... Ziemba, L. (2021). On assessing era5 and merra2 representations of cold-air outbreaks across the gulf stream. *Geophysical Research Letters*, *48*(19), e2021GL094364. Retrieved from https://agupubs.onlinelibrary.wiley.com/doi/abs/10.1029/2021GL094364 doi: https://doi.org/10.1029/2021GL094364

Sorooshian, A., Anderson, B., Bauer, S. E., Braun, R. A., Cairns, B., Crosbie, E., ... Zuidema, P. (2019). Aerosol–cloud–meteorology interaction airborne field investigations: Using lessons learned from the u.s. west coast in the design of activate off the u.s. east coast. *Bulletin of the American Meteorological Society*, *100*(8), 1511 – 1528. Retrieved from https://journals.ametsoc.org/view/journals/bams/100/8/bams-d-18-0100.1.xml doi: 10.1175/BAMS-D-18-0100.1

Sorooshian, A., Brechtel, F. J., Ma, Y., Weber, R. J., Corless, A., Flagan, R. C., & Seinfeld, J. H. (2006). Modeling and characterization of a particle-into-liquid sampler (pils). *Aerosol Science and Technology*, *40*(6), 396-409. Retrieved from https://doi.org/10.1080/02786820600632282 doi: 10.1080/02786820600632282

Stein, A. F., Draxler, R. R., Rolph, G. D., Stunder, B. J. B., Cohen, M. D., & Ngan, F. (2015). Noaa's hysplit atmospheric transport and dispersion modeling system. *Bulletin of the American Meteorological Society*, *96*(12), 2059 - 2077. Retrieved from https://journals.ametsoc.org/view/journals/bams/96/12/bams-d-14-00110.1.xml doi: 10.1175/BAMS-D-14-00110.1

Taylor, J. W., Haslett, S. L., Bower, K., Flynn, M., Crawford, I., Dorsey, J., ... Coe, H. (2019). Aerosol influences on low-level clouds in the west african monsoon. *Atmospheric Chemistry and Physics*, *19*(13), 8503–8522. Retrieved from https://acp.copernicus.org/articles/19/8503/2019/ doi: 10.5194/acp-19-8503-2019

Tornow, F., Ackerman, A. S., & Fridlind, A. M. (2021). Preconditioning of overcast-to-broken cloud transitions by riming in marine cold air outbreaks. *Atmospheric Chemistry and Physics*, *21*(15), 12049–12067. Retrieved from https://acp.copernicus.org/articles/21/12049/2021/ doi: 10.5194/acp-21-12049-2021

Wood, R. (2006). Rate of loss of cloud droplets by coalescence in warm clouds. *Journal of Geophysical Research: Atmospheres*, *111*(D21). Retrieved from https://agupubs.onlinelibrary.wiley.com/doi/abs/10.1029/2006JD007553 doi: https://doi.org/10.1029/2006JD007553

1. Methodology

1.1. In-situ aerosol measurements

A Droplet Measurement Technologies (DMT) CCN counter (Roberts & Nenes, 2005; Lance et al., 2006a) was operated in one of two modes:

(1) constant supersaturation (SS; usually set to 0.43%) or

(2) SS scanning (typically covering 0.2–0.7%; Moore & Nenes, 2009)

To compare data from all eight research flights (Section 2), we interpolate CCN from mode (2) operations to SS = 0.43% per leg using polynomial regression (described further below). We also use condensation nuclei (CN) counts of particles with diameters greater equal 10 nm via the TSI Condensation Particle Counters 3772 instrument.

1.2. Processing of ACTIVATE measurements

1.2.1. Classification of in-situ legs

Samples acquired at 1 Hz frequency are separated into flight legs, where each leg is defined as a consecutive period of CCN measurements uninterrupted by missing values (usually spanning ∼50 s periods). This separation triples the number of legs compared to using horizontal segments (cf. Sorooshian et al., 2019) and requires a refined leg type classification:

(1) Using liquid water contents (LWCs) measured by the Fast Cloud Droplet Probe (FCDP; for particle diameters 3-50 um) and the Two-Dimensional Stereo (2DS) probe (Lawson et al., 2006, produced by summing up liquid-classified particles within diameters 51-1465 um that we assume to be spherical), we define cloudy samples as those with $LWC_{FCDP} + LWC_{2DS} \geq 0.005$ g m^{-3} (e.g., Noh et al., 2013) and classify legs with at least 5 (out of ∼50) such samples as "cloudy".

(2) To classify the remaining clear legs by their relative altitude to nearby clouds, we collect the cloudy samples near each leg (within 15 min of mean leg time or within 45 min if 15 min provides fewer than 5 cloudy samples) and define the local cloud-base and cloud-top heights (CBH, CTH) from maximum and minimum altitudes, respectively, of the nearest cloudy samples (the closest 15% in time from mean leg time among samples collected) to crudely account for the spatial heterogeneity of clouds (e.g., the swiftly evolving CTH seen in Figure 1).

(3) Finally, we label each cloud-free leg by comparing its maximum and minimum altitudes (H_{max}, H_{min}) to CTH and CBH +/- a 50 m buffer to better separate FT from MBL legs and to avoid the entrainment interfacial layer (e.g., Dadashazar et al., 2018):

"clear, below-cloud":	H_{max} < (CBH - 50 m)
"clear, above-cloud":	H_{min} > (CTH + 50 m) or if H_{min} > (CBH - 50 m) and H_{max} > (CTH + 50 m) relevant for legs during ascents and descents
"clear, cloud-level":	all remaining samples above or at 500 m
"clear, near-surface":	all remaining samples below 500 m

Figure S1 shows the resulting classification for RF14, with 90 legs identified. Note that "clear, cloud-level" can appear upwind of formed clouds, intentionally marking legs that are difficult to delineate in their FT or MBL belonging.

We tested how sensitive the above setup is to selected parameters. Raising the LWC thresholds (to 0.01 g m^{-3}) would result in cloud-contaminated legs that are identifiable using leg-wise CCN spectra (not shown), while the above setup leads to satisfactory separation of "cloudy" and all other types. Using other numbers of cloudy samples to define a cloudy leg (i.e., 2 and 10 instead of 5) shifted the definition between "cloudy" and "cloud-level" legs that would have been both left out for further analysis. Parameters that defined the position of nearby clouds, however, importantly shifted the definition from "clear, cloud-level" towards "clear, above-cloud" or vice versa when using shorter (7.5 min) or longer time intervals (30 min), respectively; guided by HSRL-2 CTHs we find the above setup optimal. Using alternative percentiles (7.5 and 30 %) shifted the definition between "clear, cloud-level" and "clear, below-cloud" of two legs and had little impact of the budget analysis.

1.2.2. Projection into quasi-Lagrangian framework

In an ideal scenario for our analysis, all measurements would have been obtained in a moving Lagrangian column of MBL air as it moves downwind. Lacking such a scenario, we roughly emulate a Lagrangian framework by projecting all measurements onto a wind field and using horizontal distance from the upwind cloud edge, ΔL, as a transformed coordinate system.

From geostationary imagery we approximate a field-wide MBL wind direction from the roll orientation, assuming zero angular offset, and draw a great circle to mark the initial cloud edge (white line in Figure 1). We then use each leg's geolocation and the wind direction to determine the intercept point on the cloud edge up- or downwind of the leg coordinates and measure the geodetic distance between leg coordinates and this intercept point.

Figure 2 illustrates the resulting range $\Delta L \in [\pm 300\text{km}]$ for RF14 corresponding to the Figure 1 scene. We note that MBL wind direction and roll orientation can be offset by up to ±20-30° (Etling & Brown, 1993; Atkinson & Wu Zhang, 1996), corresponding to a range error of about ±10 km per 100 km.

1.3. MBL CCN budget

1.3.1. Entrainment

To estimate the entrainment rate (w_e) of FT air at the top of the MBL we use CO trace gas measurements (Figure S2) and rely on a simple mixed-layer approach (e.g., Lilly, 1968; Fridlind et al., 2012) to characterize the evolution of the MBL-mean mixing ratio of species X (here applied to CO to estimate the entrainment rate, and later used for the budget of $\text{CCN}_{\text{SS}=0.43\%}$). Note that we apply this approach to a horizontally translating quasi-Lagrangian domain and use MBL-averaged quantities (denoted with overbar), invoking the Lagrangian derivative:

$$\frac{d\bar{X}}{dt} = S_{\text{int}} + S_{\text{surf}} + S_{\text{entr}} \tag{1}$$

with net sources respectively from internal processes, surface fluxes, and entrainment of FT air into an MBL of depth H:

$$S_{\mathrm{entr}} = \frac{\Delta\bar{X}}{H} w_e \tag{2}$$

given the jump at the top of the MBL $\Delta\bar{X} = X_{\mathrm{FT}} - \bar{X}$ and entrainment rate

$$w_e = \frac{dH}{dt} - w_{\mathrm{LS}} \tag{3}$$

where w_{LS} is large-scale vertical wind. Internal process and surface sources are assumed zero for CO.

After combining Equations 1 and 2, we solve for w_e using the horizontal gradient in distance downwind s to evaluate the Lagrangian derivative:

$$\frac{d\bar{X}}{dt} = \frac{d\bar{X}}{ds}\frac{ds}{dt} = \frac{\bar{X}(\Delta L + 50\mathrm{km}) - \bar{X}(\Delta L - 50\mathrm{km})}{250\mathrm{km}} u \tag{4}$$

with horizontal wind speed u taken at 500 m from an ERA5 profile on 1 March 2020 20:00 UTC, at 36.90°N, 69.35°W.

In these equations $\bar{X}$, X_{FT}, and H are computed from separate 4$^{\mathrm{th}}$-order polynomial fits versus ΔL. For fitting $\bar{X}$, we use "clear, near-surface" and "clear, below-cloud", whereas for X_{FT} we use "clear, above-cloud". For CO as X_{FT} we linearly fit in-situ data (Figure S2) and for H we produce a quadratic fit of HSRL-2 (CTH, Figure S5). Once w_e is estimated, we compute S_{entr} from Equation 2 using fits to the CCN data (Figure 2).

As a check on the CO-based entrainment rates, we derive an independent estimate of w_e by first collocating GOES-16 cloud-top height (Minnis et al., 2008), available every 20 min, along ERA5-derived Lagrangian trajectories (Figure S3). Trajectories are launched hourly between 15-20 UTC from an array of starting points spanning 1x1° (Figure S3a).

Then for each trajectory, we determine dH/dt from GOES CTHs (typically increasing, as seen in Figure S3b), interpolate w_{LS} from ERA5 in time and space, and compute w_e using Equation 3. To match the quasi-Lagrangian aircraft sampling, we then extract this w_e estimate to intersect the aircraft position within tolerances of 15 km and 10 min, as shown in Figure S3c.

1.3.2. Hydrometeor collisions

We use in-situ FCDP and 2DS measurements to estimate collision-coalescence rates. After parsing the data into 5-s intervals (∼500 m horizontal distances), we bin-wise average PSDs from both instruments, and compute collision-coalescence loss rates by integrating the simplified stochastic collection equation over droplets of volume x and x' (cf. Wood, 2006):

$$\dot{N}_{\mathrm{coll}} = -\frac{1}{2}\int_0^{\infty}\int_0^{\infty} n(x)K(x',x)n(x')dxdx' \tag{5}$$

where $n(x)$ is the measured hydrometeor number concentration and $K(x,x')$ the gravitational collection kernel between droplet size bins:

$$K(x,x') = \pi[r(x)+r(x')]^2 E_{\mathrm{coll}}|v(x)-v(x')| \tag{6}$$

in which $r(x)$ the volume-mean radius for each bin, E_{coll} denotes the collection efficiencies tabulated by Hall (1980), and droplet fall speed v is computed following Böhm (1992). We follow Hall (1980) in assuming a coalescence efficiency of unity, and expect that any uncertainties or errors in the collection efficiencies are overwhelmed by the uncertainties in our stochastically constructed PSD profiles described below. Figure S5 shows two examples, demonstrating the impact of larger hydrometeors, as well as the estimated contribution to $\dot{N}_{\mathrm{coll}}$ from riming (cf. Tornow et al., 2021) roughly estimated by summing over bins with frozen hydrometeors using the same kernel.

To obtain MBL-mean collision-coalescence rates some assumptions must be made about the vertical structure of clouds within the MBL given sparse aircraft sampling. Here, we assume in-situ measurements constitute a representative collection of samples of the actual MBL that is characterized by a single, vertically contiguous cloud layer that evolves with fetch. We account for this evolution by using HSRL-2-based CTH and RSP-retrieved liquid water path (LWP) values projected onto the semi-Lagrangian framework (Section S1.2.2) to derive synthetic cloud profiles with stochastically drawn in-situ intervals that satisfy some proximity criteria.

We begin with RSP LWP retrievals. Discretizing the atmosphere into 50-m thick layers, we start at the layer closest to cloud top (from median of HSRL-2 CTH values within 100 s of an RSP measurement) and consider in-situ data for stochastic sampling obtained vertically within 50 m of the layer, within 100 km horizontally of the RSP observation, and within 15 min of RSP acquisition. If these criteria produce no samples, we double proximity thresholds and, if still short on samples, drop the vertical proximity requirement. Once a layer is assigned a PSD, we proceed downward until the vertical LWC integral matches the RSP LWP, but not past cloud base (the lowest layer in which clouds were observed in-situ, $\sim$700 m for RF14). For large LWP values ($>$300 g m^{-2}), the cloud thickness is insufficient and though the reconstructed LWPs fall short, they are retained (Figure S4, right panel). Figure S4 also shows all stochastically generated profiles versus ΔL and Figure S6 shows details of one example profile. The proximity criteria yield a reasonable subset of in-situ observations for sampling (black dots in Fig. S6) and prevent sampling from regions that are different in character (e.g., stemming from a progressively deepening MBL with N_d diminishing downwind). To match other budget terms we compute a 100-km running mean excluding cloud-free gaps.

Unfortunately, RSP only provides LWP values where the sun-observer geometry is favorable. For the case shown in Figure 1, these correspond to the northwest-most leg, highlighted gray. As described further below, we use MODIS LWP retrievals (at 1730 UTC) to extend the analysis downwind.

We tested the sensitivity of the selected setup. Data collection over alternative time intervals (2.5 and 10 s instead of 5 s) and other vertical meshes (25 and 100 m) leave the budget analysis unaffected. Halving or doubling the proximity criteria affect the budget mostly beyond $\Delta L = 100$ km (reducing and increasing $\dot{N}_{\mathrm{coll}}$, respectively) by restricting availability to downwind samples that include larger hydrometeors.

1.3.3. Uncertainty

To estimate uncertainties, we apply Gaussian error propagation. Individual uncertainties associated with $\bar{X}$, X_{FT}, and z_i are taken from each fit's 95% confidence interval. These errors dominate when used in differentials, such as equation 3 (e.g., for $\dot{N}_{\mathrm{tot}}$ shown as dark blue bar in Figure 4). We assume 10-km uncertainty for ΔL, as described in Section S1.2.2. Assumed errors for ERA-5 variables are 10% (Seethala et al., 2021; Li et al., 2021). The error for $\dot{N}_{\mathrm{coll}}$ is estimated as the standard deviation across the locally available population, chosen because substantial sample variability (Figure S6) likely exceeds conventional error propagation. Similarly, we estimate uncertainties of median satellite-based entrainment rates as the range between 5^{th} and 95^{th} percentiles across individual trajectories (which exceed conventional error propagation) to account for a high bias of GOES CTH compared to HSRL-2 that shoud leave median entrainment rates unaffected.

Table S1. 2020 ACTIVATE CAO research flights, the prevalent MBL wind direction, coordinates defining the initial cloud edge, and instrument limitations relevant to this study (see text), such as the availability of the Research Scanning Polarimeter (RSP).

Date / Number	#	Wind Dir.	Cloud edge coordinates	Instrument Limitations
2020-02-21 / 1	RF04	20°	38.0°N 76.4°W – 39.5°N 72.0°W	Falcon only
2020-02-22 / 1	RF05	25°	34.0°N 77.4°W – 38.0°N 71.5°W	Falcon only
2020-02-22 / 2	RF06	25°	34.0°N 77.4°W – 38.0°N 71.5°W	Falcon only
2020-02-27 / 1	RF09	300°	34.0°N 76.0°W – 38.0°N 73.0°W	/
2020-03-01 / 1	RF13	315°	35.0°N 75.0°W – 40.0°N 72.0°W	/
2020-03-01 / 2	RF14	315°	35.0°N 74.0°W – 40.0°N 72.0°W	/
2020-03-08 / 1	RF17	10°	33.0°N 77.0°W – 36.5°N 72.0°W	No RSP
2020-03-08 / 2	RF18	20°	34.5°N 78.0°W – 34.5°N 70.0°W	No RSP

Table S2. Instruments, products, and estimated uncertainty used.

Instrument (in-situ)	**Used Products**	**Uncertainty**	**Reference**
DMT CCN Counter	CCN(s), for either SS=0.43% or SS $\in$ [0.2,0.7%]	ΔSS=0.04, δCCN=10%	Lance, Nenes, Medina, and Smith (2006b)
TSI CPC-3772	CN-10nm	10%	/
TSI LAS	dNa/dlogD for D $\in$ [0.1,3.1 um]	20%	Froyd et al. (2019)
SMPS	dNa/dlogD for D $\in$ [0.003,0.089 um]	20%	Moore et al. (2017)
PILS	Mass conc. for D $\in$ [0.05,4.00 um]	/	Sorooshian et al. (2006)
AMS	Mass conc. for D $\in$ [0.06,0.60 um]	<50%	DeCarlo et al. (2008)
SPEC FCDP	dNd/dlogD for D $\in$ [3.0,50 um], LWP	/	Knop, Bansmer, Hahn, and Voigt (2021)
SPEC 2DS	dNd/dlogD for D $\in$ [30,1460 um], LWP, IWC	/	Lawson et al. (2006) Kleine et al. (2018) Taylor et al. (2019)
PICARRO G2401-m	CO gas concentration	2%	/
Instrument (remote)			
HSRL-2	Cloud-top height		Burton et al. (2018)
RSP	Cloud optical thickness, Droplet effective radius	15%	Cairns, Russell, and Travis (1999)
Dropsonde	Temperature, Pressure	0.2 K and 0.05 hPa	Hock and Franklin (1999)

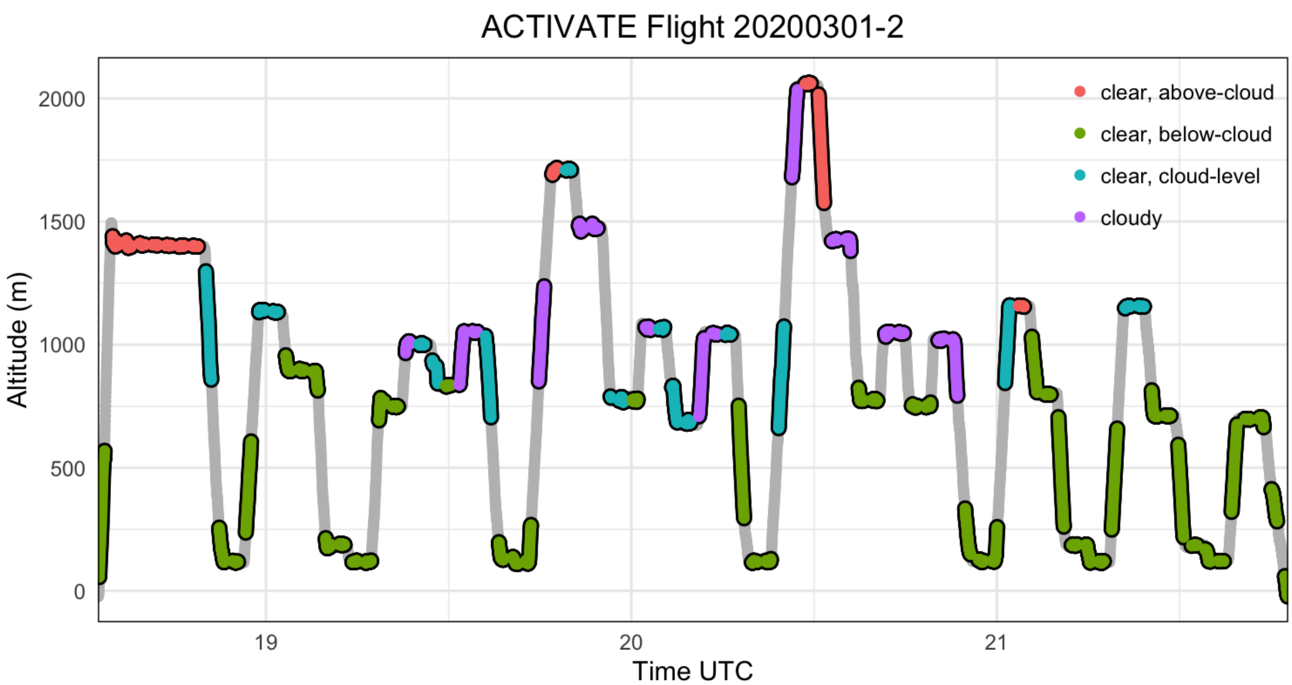

Figure S1. Categorization of CCN measurements during RF14 on 1 March 2020 as defined in Section S1.2.1

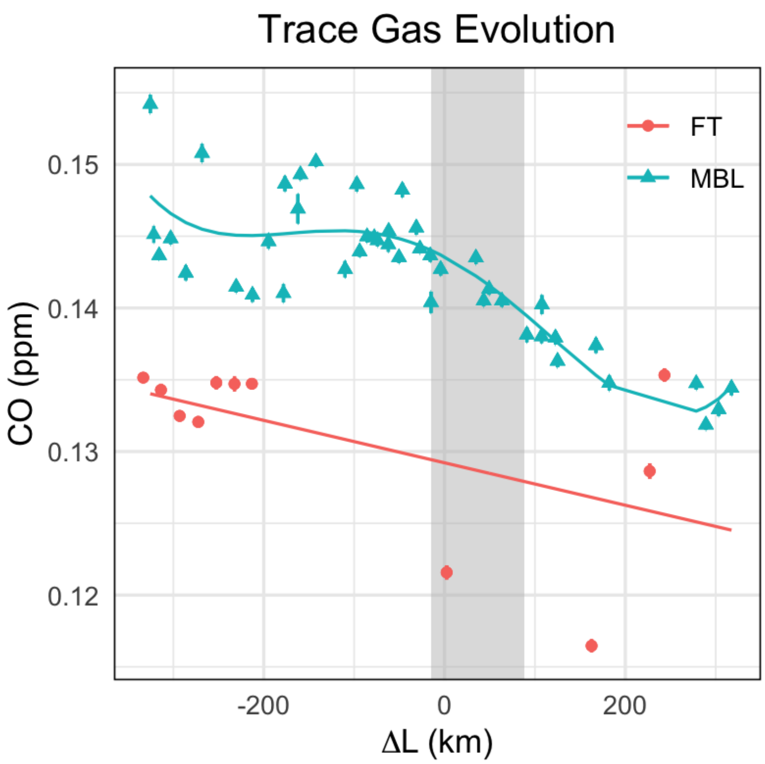

Figure S2. CO trace gas measurements during RF14 on 1 March 2020 sampled in the FT or MBL (see legend) as a function of distance from cloud edge (ΔL) used to estimate entrainment rates (Figure 4a). Gray shading indicates distance range of budget analysis using RSP. Vertical bars show the standard error.

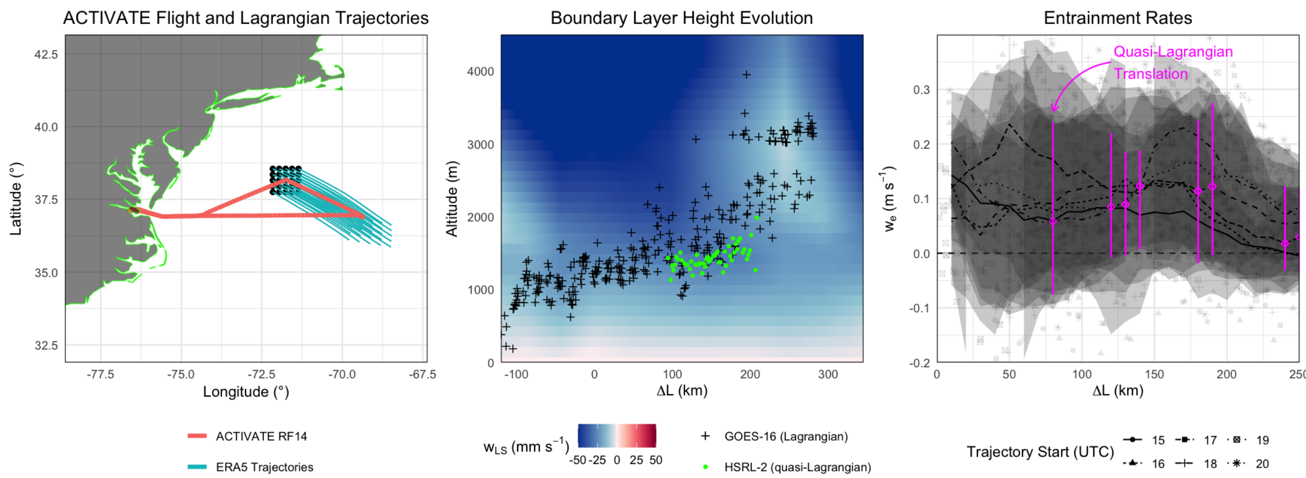

Figure S3. An array of ERA5 Lagrangian trajectories (left) launched at 1900 UTC on 1 March 2020, collocated CTH with fetch (middle) that were retrieved from GOES-16 satellite observations (black crosses) and from HSRL-2 (green filled circles) with ERA5 large-scale vertical wind fields (color shading), and derived entrainment rates versus fetch (right) for different launch times that intersected the flight track at different fetch values (magenta). Semi-translucent, gray shading and vertical bars (magenta) highlight 5th to 95th percentiles of entrainment rates obtained across the array of trajectories.

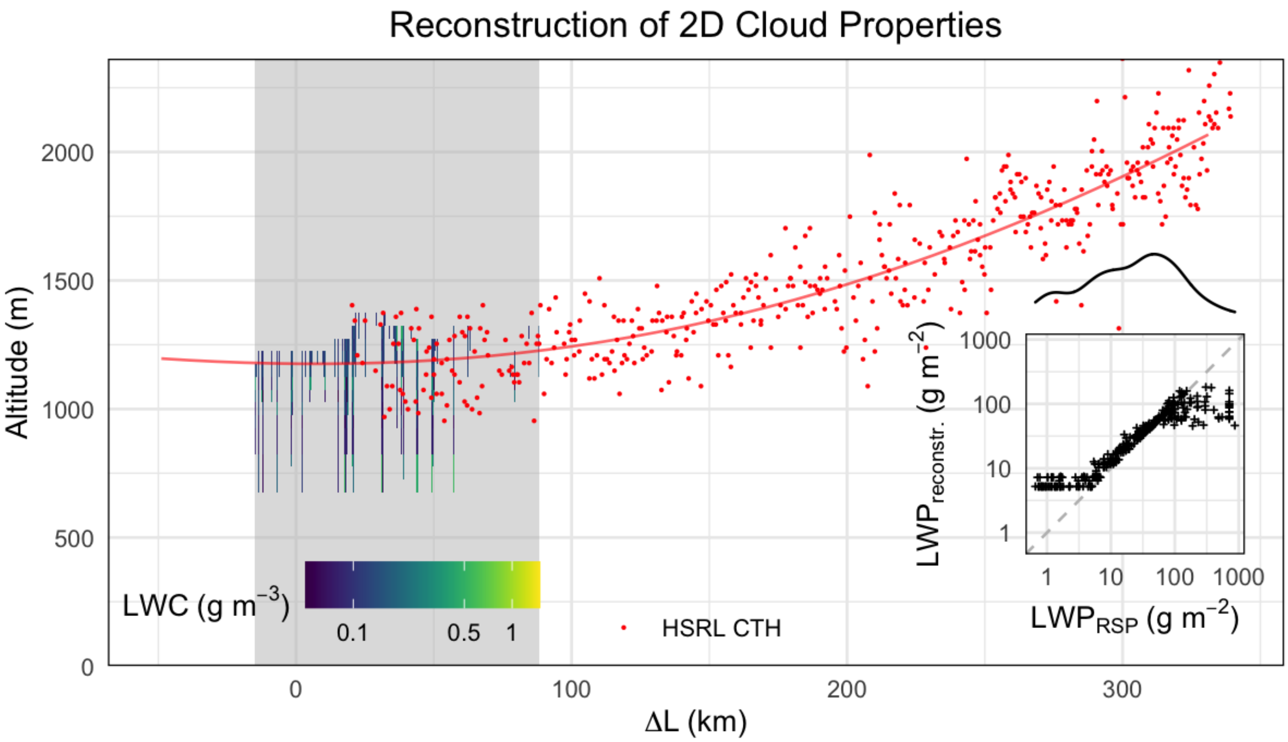

Figure S4. Overview of RF14 (1 March 2020) mock-cloud-profiles (LWC shown as colored shading) together with HSRL-2 cloud-top heights (red dots) and its quadratic fit (red line). The inset compares LWP from reconstructed profiles with the RSP-based LWP values. The curve above the inset panel indicates the probability density function for RSP-based values.

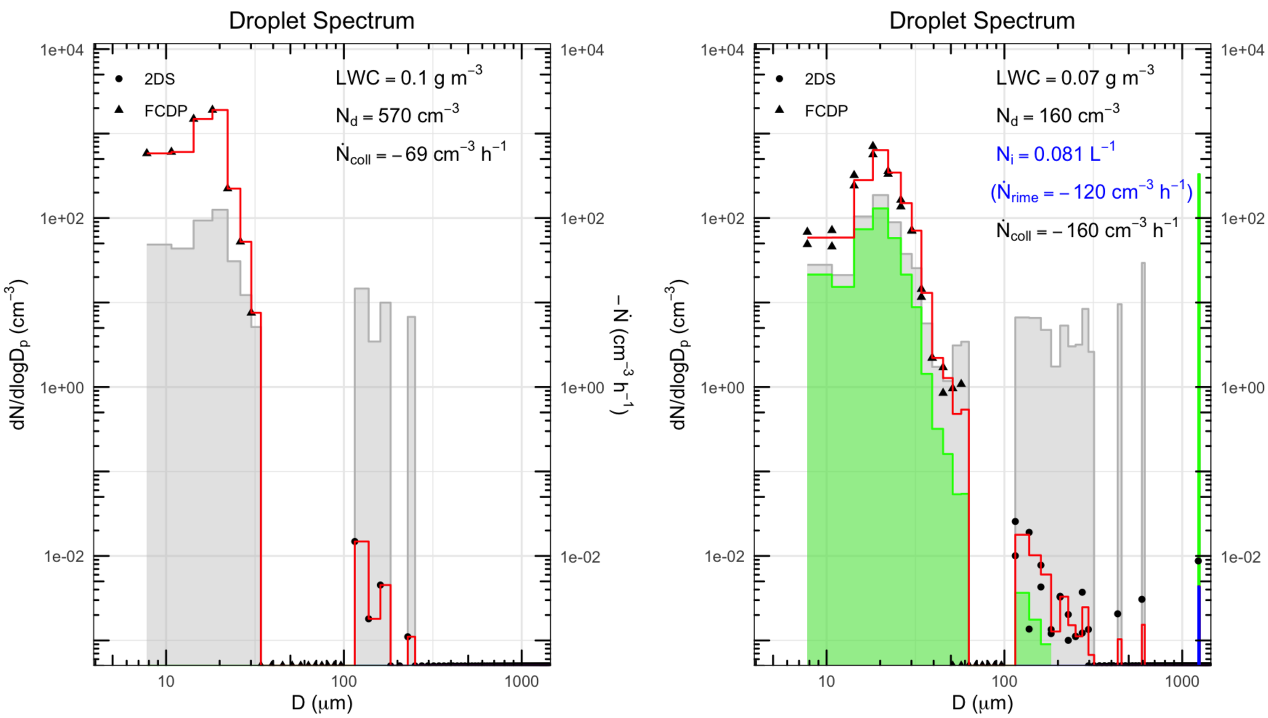

Figure S5. Example hydrometeor size distributions (red, scale on left axes) during RF14 at two flight times 70495 s (left) and at 73525 s (right) and corresponding computed collision loss rates (listed at top-right corner) with bin-wise contributions (gray shade, scale on right axes). Rates that involved hydrometeors classified as frozen (only in one bin, shown with blue bar) are labelled as "riming" (shown as integral in blue text and as bin-wise contribution through green shading) and are simply obtained by using Equation S5 and ignoring all liquid-liquid interactions.

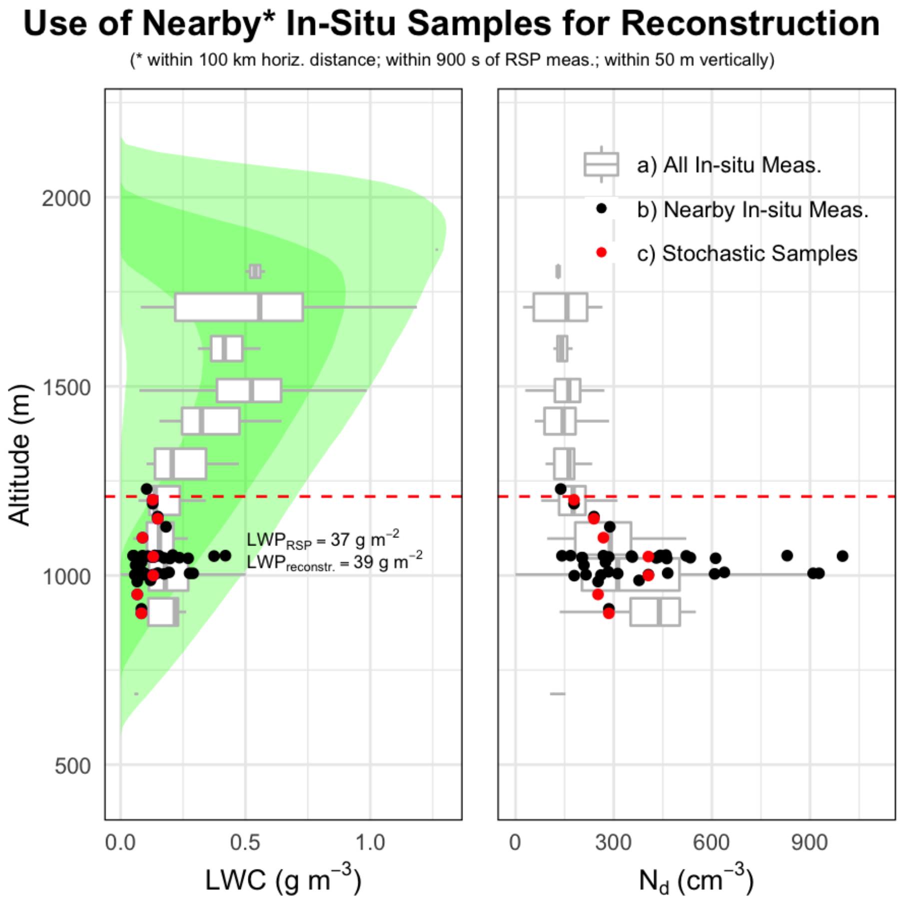

Figure S6. Example of RF14 (1 March 2020) in-situ samples (black) to stochastically build a mock-cloud-profile (red), shown for LWC (left) and N_d (right), until the LWP roughly matches the nearby RSP-sampled value. Gray bars mark the range of all in-situ observations (box ranging between 25th and 75th percentiles and whiskers extending to 5th and 95th percentiles). The green shading (lighter shade marks 5th to 95th and darker shade 25th to 75th percentiles) shows LWC profiles from large-eddy simulations of a similar case (altitudes shifted 500 m downward to match the prevalent MBL height). The decrease of N_d with height is an artifact of MBL deepening downwind where N_d progressively decreases.

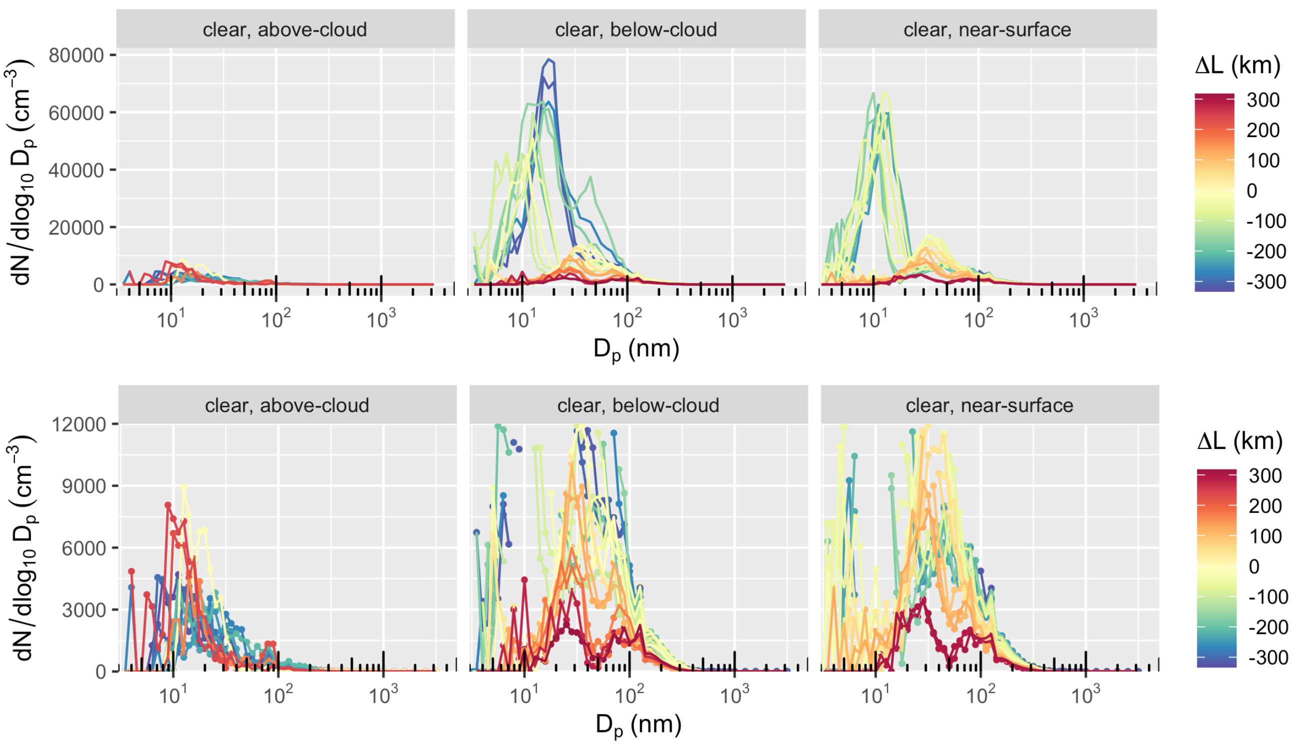

Figure S7. Aerosol particle size distributions measured during RF14 (1 March 2020) in the FT and MBL (top; and with reduced y-axis range, bottom). Colors mark the downwind distance from cloud edge, ΔL.

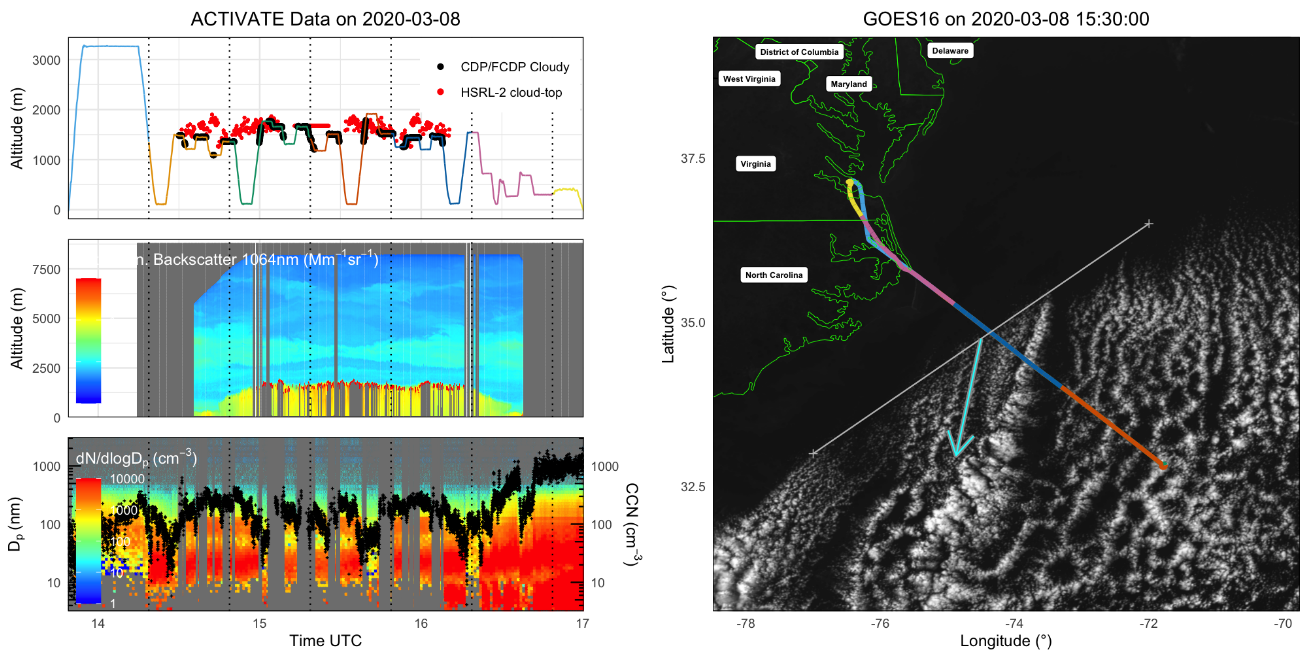

Figure S8. As in Figure 1, but for the first research flight on 8 March 2020 (RF17).

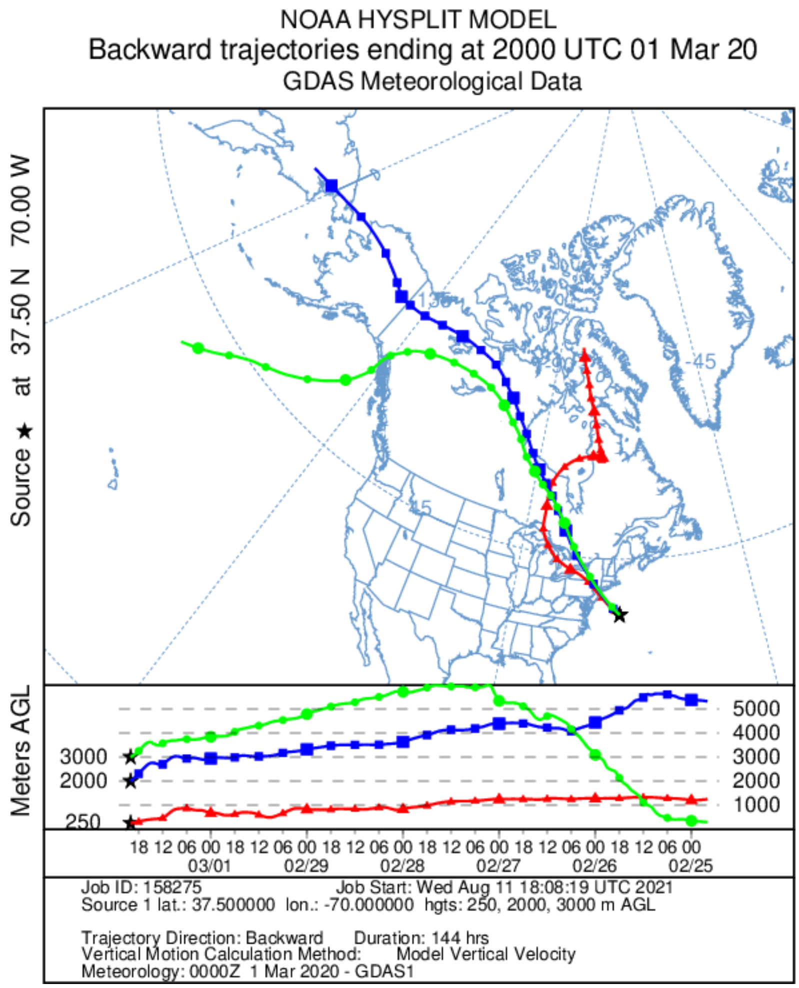

Figure S9. Back-trajectories based on HYSPLIT (Stein et al., 2015; Rolph et al., 2017) for RF14.